Nuclear Engineering and Technology 54 (2022) 3205–3214

Contents lists available at ScienceDirect

Nuclear Engineering and Technology

journal homepage: www.elsevier.com/locate/net

Original Article

Effect of post processing of digital image correlation on obtaining accurate true stress-strain data for AISI 304L

Olivia Angel [a, *], Glynn Rothwell [a], Russell English [a], James Ren [a], Andrew Cummings [b]

[a] Faculty of Engineering and Technology, Liverpool John Moores University, James Parsons Building, Byrom Street, Liverpool, L3 3AF, UK
[b] Nuclear Transport Solutions, Hinton House, Birchwood Park Avenue, Risley, Warrington, Cheshire, WA3 6GR, UK

ARTICLE INFO

Article history:
Received 9 December 2021
Received in revised form
18 March 2022
Accepted 27 March 2022
Available online 13 April 2022

Keywords:
Fracture
Digital image correlation
Uniaxial tension
Stress-strain curves

ABSTRACT

The aim of this study is to provide a clear and accessible method to obtain accurate true-stress strain data, and to extend the limited material data beyond the ultimate tensile strength (UTS) for AISI 304L. AISI 304L is used for the outer construction for some types of nuclear transport packages, due to its post-yield ductility and high failure strain. Material data for AISI 304L beyond UTS is limited throughout literature. 3D digital image correlation (DIC) was used during a series of uniaxial tensile experiments. Direct method extracted data such as true strain and instantaneous cross-sectional area throughout testing such that the true stress-strain response of the material up to failure could be created. Post processing of the DIC data has a considerable effect on the accuracy of the true stress-strain data produced. Influence of subset size and smoothing of data was investigated by using finite element analysis to inverse model the force displacement response in order to determine the true stress strain curve. The FE force displacement response was iteratively adapted, using subset size and smoothing of the DIC data. Results were validated by matching the force displacement response for the FE model and the experimental force displacement curve.

1. Introduction

Nuclear transport packages must pass rigorous post design safety tests before they can be licenced for use. The packages are assessed on their ability to endure the cumulative effects of a series of tests to ensure they are able to withstand and respond to any serious accidents, preventing any radiation leaks [1,2]. Breach of the outer shell during a series of drop tests may lead to the failure of the package during subsequent thermal tests, by prolonging the burning of internal shielding materials. Finite element models are utilised for demonstrating the performance of nuclear transport packages. Current finite element models accurately reproduce elastic material response and also predict the materials response in the plastic regime up to the ultimate tensile strength (UTS). A materials UTS is the maximum stress that it is able to withstand whilst under loading. Standard tensile testing of a material to produce a typical elastic-plastic material model is insufficient to predict the stress-strain response beyond UTS. Therefore, the accuracy of the multiaxial plasticity response beyond UTS is unknown. Obtaining stress-strain response beyond UTS will contribute material data and fracture behaviour, aiding the design of nuclear transport packages.

Uniaxial tensile tests are used to determine a materials characteristics by observing the materials response when subjected to a load. This is broken down into elastic and plastic regions. Beyond the necking region, strain is non-uniform along the gauge length. Literature suggests that in order to determine stress and strain data within the necking region, two methods can be used, inverse or direct. The inverse method incorporates experimental measurement with finite element (FE) analysis to determine the true stress-strain curve [3]. Whereas, the direct method uses instantaneous measured parameters from the surface of the specimen. The inverse method has been researched extensively [4–6]. In this method a reference stress-strain curve was iteratively adapted to reduce the divergence between the experimental data and FE analysis. Kamaya and Kawakubo [7] proposed a methodology which used the inverse process, to determine the true stress-strain curve of an hourglass type specimen with a range of FE analysis and digital image correlation (DIC). Implementing the inverse method is complex when compared to the direct method.

* Corresponding author.
E-mail address: o.s.angel@2019.ljmu.ac.uk (O. Angel).

https://doi.org/10.1016/j.net.2022.03.038

DIC is the application of non-contact methods, that utilises random patterns to compare sub-regions, obtaining a full-field of data during testing of structural components [8]. Strain gauges and extensometers provide a single dimension of strain or displacement. DIC has advantages compared to extensometers and strain gauges, as it is possible to assess more complex geometries due to it being a non-intrusive, non-contact method. A range of measurements can be provided from DIC, such as displacements and strains across the material, capturing various data from deformation testing up to failure. Optical methods of stress analysis became a major research topic following the development of interferometry. Application for optical testing was created when Twyman and Green [9] used a modified Michelson interferometer to test optical components. Peters and Ranson [10] were among the first to introduce digital image techniques as they are currently known. They suggested the simplest approach for displacement measurements, is to correlate two speckle images mathematically in a similar process used for area correlation in pattern recognition. This method incorporates a system allowing the cross-correlation of a reference scene with a stored image. The utilisation of DIC was further established when Sutton et al. [11,12] conducted experiments for the application of DIC methods. The researchers formed the basis of methods presently used for DIC. The experiments set up used a random speckled pattern and digital video acquisition to find parameters of interest for problems regarding rigid body dynamics. In recent studies, DIC is frequently used throughout experiments within failure mechanics. Researchers such as Bai [13], Mohr and Ostwald [14], Dunand and Mohr [15], H. Ghadbeigi et al. [16] have used DIC to obtain material failure data for a range of geometries and loading conditions.

The direct method uses instantaneous measured parameters, optical systems such as DIC can be used. DIC can produce data throughout testing, allowing for measurements such as true strain and instantaneous cross-sectional area up to failure to be extracted. With this data the true stress can be calculated. Li et al. [17], used DIC to determine the true stress-strain curve of advanced high-strength steel D9780. Results were validated by comparing the direct approach to a range of methods, which found that the direct measurement method delivered a more accurate stress-strain curve at large strains. Literature on the direct method [18–20] is limited. Previous work cited relating to the direct method did not present much detail for different parameters, such as various subset sizes or filtering options. However, subset sizes ranging from 21 × 21 pixels to 81 × 81 pixels, with increments of 6 × 6 pixels were investigated by Yaofeng and Pang [21]. The results found the optimal subset size is a trade-off between the influence of random errors and systematic errors. A study investigating different filtering strategies used adaptive low-pass filters and notch filters to eliminate noise, although this type of filtering was found to increase errors [22]. There is no study that has investigated the effect of subset size and the parameters used during the post processing of DIC data. This gap in research has been investigated in this paper and is of importance in order to determine accurate stress-strain data.

The basic principles of DIC are relatively simple. Displacements are determined from a set of images taken before and during deformation of a specimen's surface, which typically has a distinguishable speckle pattern. Assumptions are made that features of the structure surface are displaced together and are preserved after deformation [23].

A subset (also known as facet) is a portion of the speckle pattern, which is selected during the reference state for the calculation of the displacement throughout testing. The initial position of the subset from the reference image is matched to the deformed subset. To track numerous subsets DIC uses matching criteria to calculate a field of displacements. A predefined matching criterion (also known as the correlation criterion) and a optimisation algorithm is needed during the DIC process. Robustness, computational cost and reliability of a matching criterion are of great importance as deviations during experiments such as unstable or uneven lighting and non-uniform contrast may occur [24]. Sutton et al. stated that the method of DIC owes its name to the cross correlation (CC) criterion [8]. However, the CC criterion is one of many matching criteria. Literature includes a variety of additional criteria such as; sum of absolute difference (SAD), sum of squared difference (SSD), and parametric sum of squared difference (PSSD) [8,25,26].

Fundamentally, matching criteria must reduce the difference between the reference and moved subset. SSD Criteria is shown in Equation (1). For the reference subset (as shown in Fig. 1) $F(x_i, y_i)$ and the moved subset $G(x_i^*, y_i^*)$, represent the greyscale intensity of the i th pixel. This can be further simplified from $F(x_i, y_i)$ and $G(x_i^*, y_i^*)$ to F_i (greyscale intensity for reference subset) and G_i (greyscale intensity for deformed subset) respectively [23,25].

$$\sum (F_i - G_i)^2 \tag{1}$$

For CC criteria when $\sum F_i G_i = 1$, the greyscale intensity distributions of the two subsets are the same. Thus, the closer to 1 the correlation coefficient is, the higher accuracy of match of the subsets obtained. Minimisation of the SSD criteria is mathematically equivalent to the maximisation of the CC criteria [25]. The software used in this project provided by Dantec Dynamics uses PSSD. The generalised $PSSD_{ab}$ coefficient (as shown in Equation (2)) has unknown parameters a and b to resolve for both the offset and scale changes of the intensity of the target subset.

$$\sum (aF_i + \mathrm{b} - G_i)^2 \tag{2}$$

The evaluated data can be displayed and analysed within the DIC software used and the data required can be extracted by using gauge visualisation parameters. Gauge visualisation parameters offers the prospect for defining areas and points on the specimen's surface to obtain data such as displacement and strain. The software has three options for different parameters, by either using a gauge point, a polygon or a line.

Selecting the subset size is important as each subset is solved individually, the contrast within a subset is essential to ensure the pattern is matched. The distance between subsets is controlled by the grid spacing. The overlap of subsets is used to increase the spatial resolution [27]. This means that the size of a subset is

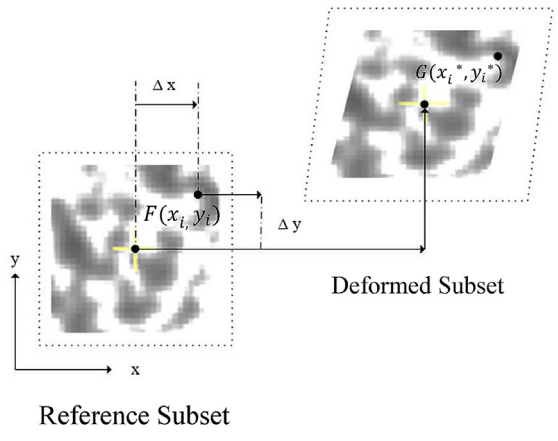

Fig. 1. Deformation of subset before and after.

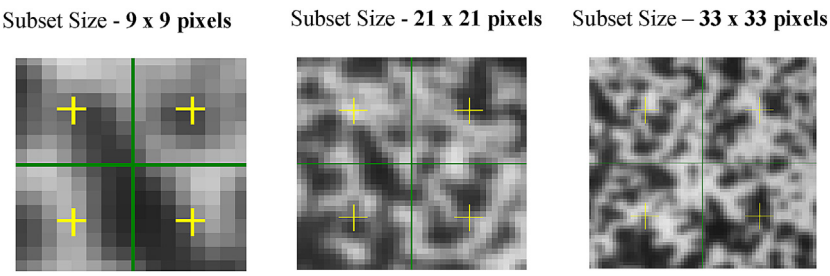

Fig. 2. A range of subset sizes for the same speckle pattern.

determined by the speckle pattern and must contain more than one speckle [28].

There are four main attributes that make a speckle pattern; contrast, size and speckle edge and density. There is not one speckle pattern that can be used for all testing, because what is suitable for one test may not be for others. The purpose of a speckle pattern is to work in conjunction with lighting conditions to create a digital image that is a random, high-contrast, low noise pattern. Increasing the gain of the camera will amplify the signal increasing the number of counts recorded by the camera, however this also generates more noise in the image [29].

The cameras used for testing have a resolution of 2448 × 2048 pixel (px). Different images will be generated depending on the area covered, meaning there will be a difference in size of a speckle pattern when using the same pixel area. Various subset sizes for the same speckle pattern are shown in Fig. 2. For the subset size 9 × 9 pixels the evaluation would not complete as each subset does not contain enough contrast, compared to subset size 21 × 21 pixels and 33 × 33 pixels.

The influence of subset size on the quality of data is shown in Fig. 3, this graph shows the approximated statistical error radius depending on the subset size. As the subset size was increased, the error was decreased for both the reference step and also at the onset of failure. Researchers Hunady et al., also concluded the biggest error radius is estimated by using smaller subset sizes [30].

During evaluation of the data, the DIC software has a smoothing tab that defines the method and the strength of the smoothing of data. Strain can be found by calculating the gradient of the deformation. If no filtering is applied to an evaluated data set, strain will only be calculated by the distortion of the subset.

There are two filters to choose from;

1. Local regression filter - Which is based on adaptive spline polynomial algorithm (ACSP). The strength of the smoothing for a local regression filter is defined by the kernel size.

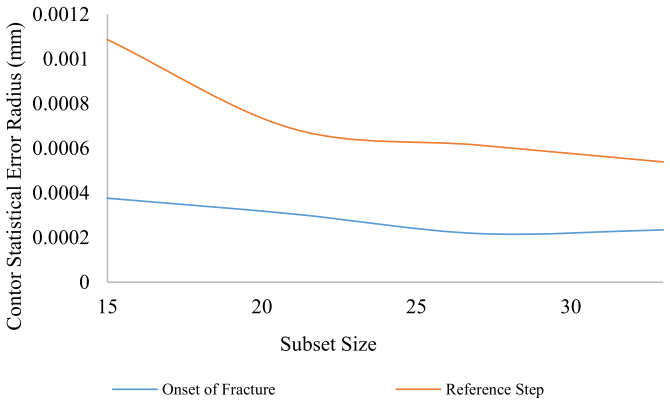

Fig. 3. Influence of the subset size on the contour statistical error radius.

2. Smoothing spline filter - The strength of smoothing for a spline filter depends on two parameters:
   - o The grid reduction factor - Changes the density of the grid points relative to the data grid, increasing this constraint means less grid points.
   - o The smoothness factor - Restricts the global curvature, by increasing this parameter the data will also be more smoothed.

Filters should be used with caution, whilst an increased filter smooths out the data and reduces the standard deviation of the data, it also decreases the spatial resolution. Spatial resolution is important as it determines the level of detail, regarding an object, which can be extracted from the image [31,32].

Material data for AISI 304L beyond UTS is limited throughout literature. True stress-strain curves to failure for AISI 304L were produced by Blandford et al. [33]. However, the research stated that tensile testing did not include a method of continuous monitoring of the neck area, but used extrapolation to the fracture point. Extrapolation method is regularly used to extend true stress-strain data past the uniform elongation and occasionally those extrapolations are based on an arbitrary assumption [17]. This research proposes using the direct method to obtain three parameters needed to determine true stress-strain data; displacement, cross section area (of necking region) and true strain until the onset of failure. Post-processing DIC results is of importance, as different filtering and/or subset size results in different true stress-strain curves. Literature available shows there is insufficient research carried out to compare the variation in parameters. The aim of this paper is to not only extend data available post UTS for AISI 304L, but to provide a clear and accessible method to obtain accurate true-stress strain data. Validation is achieved by matching the force displacement curves from the experimental tests.

2. Methodology

In order to accurately determine the required true stress-strain data, post-processing of the DIC data will be used in an FE analysis to be compared to the experimental force displacement response. The approach is briefly described below:

1) Perform a series of experimental tensile tests using DIC, taking a series of images throughout testing until failure.
2) Determine the onset of failure.
3) Determine which gauge visualisation parameters to use to extract data.
4) Plot an experimental force displacement response.
5) Decide subset size and filtering parameters to run evaluation.
6) Determine the instantaneous cross sectional area and true strain in order to plot a true stress-strain curve.
7) Input the true stress-strain data and displacement at failure (from DIC) into FE model and run analysis.

Table 1
Chemical composition and material properties of AISI 304L

Tensile Strength (MPa)		Yield Point (MPa)				Elongation (%)	
(R_m)		($R_{p(0.2)}$)		($R_{p(1.0)}$)		(A_5)	
547		242		283		55	
Carbon *(C)*	Manganese *(Mn)*	Silicon *(Si)*	Phosphorous *(P)*	Sulphur *(S)*	Chromium *(Cr)*	Cobalt *(Co)*	*Nitrogen (N)*
0.012%	1.08%	0.27%	0.028%	0.001%	18.7%	0.12%	0.07%

8) Plot the force displacement response for the FE model and compare to the DIC force displacement curve. If they match, then the true stress-strain data is correct and the analysis accurately replicates the experiment. If the curves do not match, then steps 5 to 8 must be repeated.

3. Experiments

3.1. Experimental test

Tensile specimens were tested on an Instron Servo Hydraulic testing machine using displacement control at a rate of 5 mm/min. The material used for the experiments was AISI 304L, which is used for the outer construction of nuclear transport packages. This material has been used extensively for the manufacture of containers throughout history due to its material properties. The chemical composition of AISI 304L is shown in Table 1. The DANTEC digital 3D Image correlation system Q-400 and Istra4D software was used. The experimental setup is shown in Fig. 4.

Before the experimental test takes place the testing equipment was rigidly mounted to ensure both cameras were fixed together to reduce relative camera motion. In order to level the DIC equipment and to centralise cameras, a laser level and a target grid were used. Data acquisition systems were configured such that the recording procedure and the DIC software was synchronised with the force output from the testing machine.

Design of DIC measurements are summarised in Table 2. The cameras and external lighting remained the same throughout, a 50 mm lens with an additional 5 mm extension tube were used to ensure that the field of view (FOV), accounts for the specimens region of interest (ROI) to deform and remain in view. The specimen required a large depth of field (DOF) in order to keep all of the geometry in focus. Thus, the maximum F-Stop 16 was used. Aperture was fixed depending on the ideal DOF for the specimen, exposure time and external light were used to restrict motion blur and achieve sufficient contrast.

Speckle pattern was generated using spray paints. Before the painting process the specimens were thoroughly degreased using isopropyl alcohol cleaner. The average speckle pattern size was approximately 8 pixel/0.2 mm.

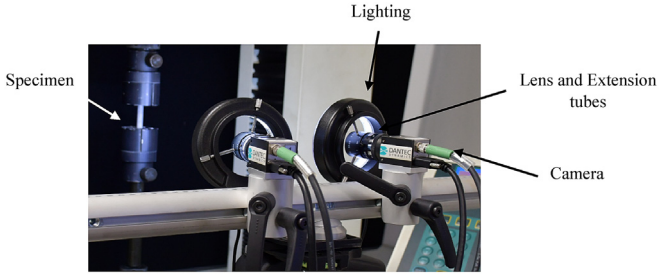

Fig. 4. Dantec dynamics experimental DIC set up.

Table 2
DIC measurement parameters and equipment.

Name:	Value:
Stereo Angle	15
Stand-off Distance	500 mm
Field of View	Approx. 70mmx70mm
Exposure Time	70 ms
Lens	50 mm
Extension Tubes	5 mm
Aperture	16 f-stop
Calibration Target	20 mm -GL-06-WMB 9X9

Static images were taken before the calibration to highlight issues, including any glare, defects in speckle pattern and uneven lighting distribution. Following this, a series of images of a calibration target were taken for a range of orientations. This allowed for all the intrinsic and extrinsic camera parameters to be found, by extracting data points from the pattern on the target. Intrinsic parameters relate a single camera image to the physical world, thus applying to both 2D-DIC and stereo-DIC. Intrinsic parameters include; focal length, image centre and scale. For a stereo rig set up the extrinsic parameters are used to determine the relationship between the cameras coordinate system for triangulation. Extrinsic parameters include; stereo-angle, baseline, stand-off distance [34,35]. Post calibration images were then taken to ensure that there were sufficient grid points distributed over the region of interest on the specimen. As the experiment started, a reference image was taken, followed by a series of images using a recording procedure until fracture occurred and the test was stopped.

3.2. Specimen

The design of the cylindrical dog-bone tensile specimens were based on the British Standards: ISO 6892–1:2019, the dimensions in mm are shown in Fig. 5 [36]. The manufacture of the specimens was from a 250 mm × 20000 × 60000 mm plate.

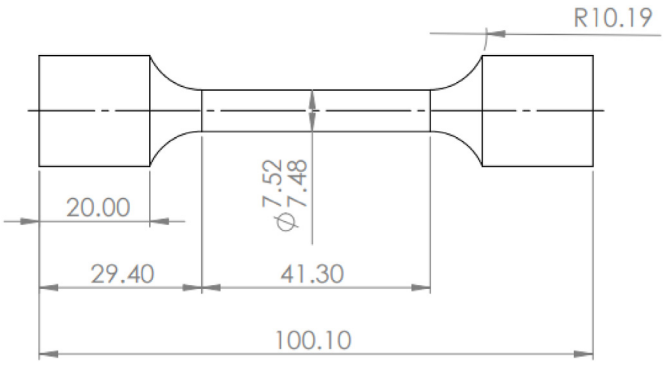

Fig. 5. Tensile specimen dimensions.

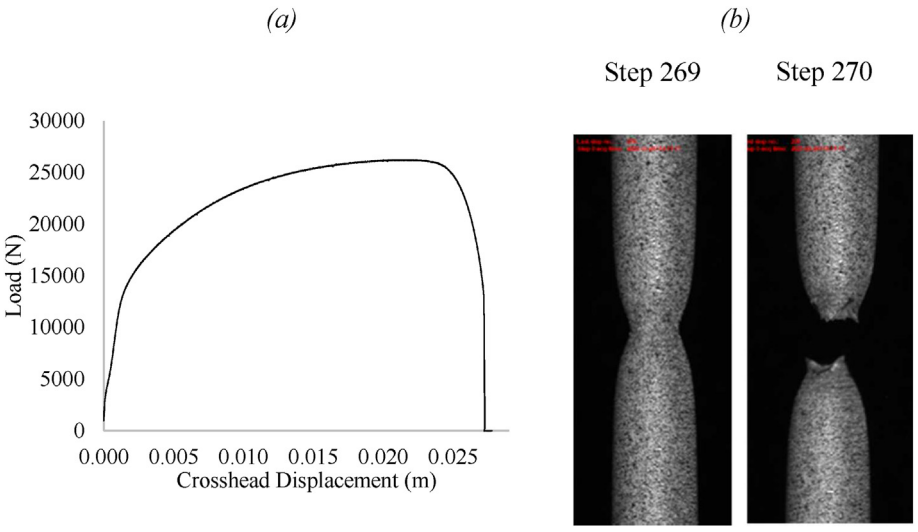

Fig. 6. a) Force-crosshead displacement graph using machine data b) Fracture initiation of tensile and failure of specimen.

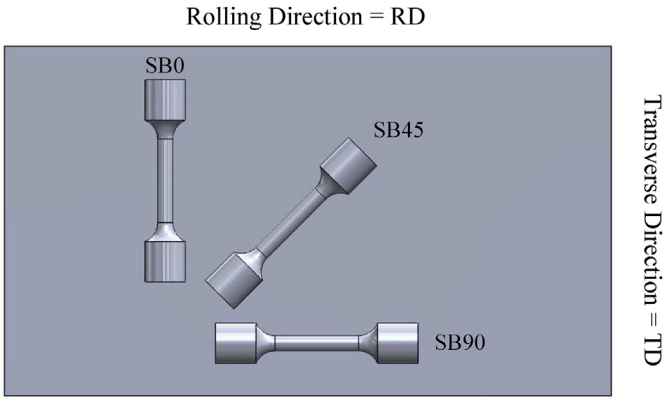

Fig. 7. Rolling directions of tensile specimens.

4. Results and discussion

4.1. The onset of failure

Physical changes at microscopic and macroscopic levels are used as indicators to predict the onset of fracture. Microscopically, ductile materials are subject to damage mechanisms such as shear decohesion, nucleation, growth and coalescence of voids until final fracture. Whilst macroscopically, the material stiffness and strength of ductile materials decreases [37]. In order to determine the failure strain, fracture initiation must first be determined.

Researchers Bao and Wierzbicki [38] used observations from both experimental and FE analysis to determine critical locations of fracture initiation. The definition for fracture initiation was dependent on the range of stress states. Significant load drops in the force–displacement responses were used as the fracture initiation for the tensile and shear tests.

Dunand and Mohr [5] defined the instant of onset of fracture not by the location, but by the first detectable discontinuity at the specimen surface. FE simulations were performed of each experiment. It was assumed that the location of the onset of fracture concurred with the position of the highest equivalent plastic strain, within the specimen at the moment of fracture initiation.

Baltic et al. [39] planned to specify fracture strain based on the first detectable incoherence in the surface displacement field, following Dunand and Mohr. However, the researchers found their experiments did not show such a clear connection and no sudden drop in the load displacement curve was observed. Therefore, they defined fracture strain as the maximum local equivalent plastic strain just before the instant of the final failure of the specimen.

In this study, fracture initiation of the tensile specimens was shown by the load drop in Fig. 6a and the moment of fracture initiation was found when post processing using the DIC software. During the post processing of the data the accuracy was set to 0.1 pixels. The image number taken during testing is referred to as the step. For example, Fig. 6b shows step 269 and step 270, where step 269 will be taken as the onset of failure.

The sudden drop in the load displacement curve matches the

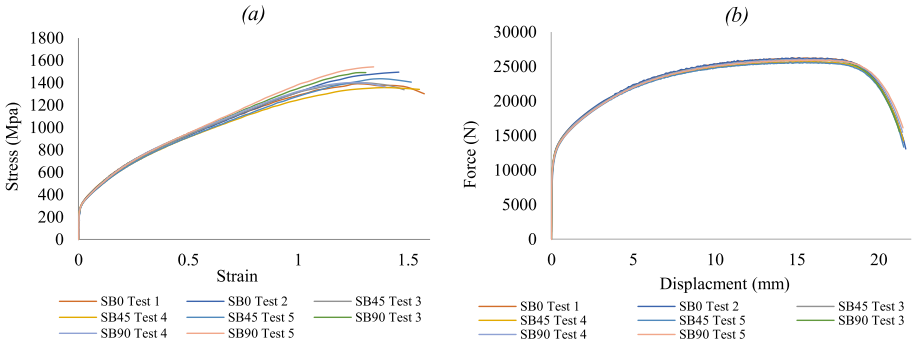

Fig. 8. a) Force displacement curves b) True stress-strain curves for a range of rolling directions.

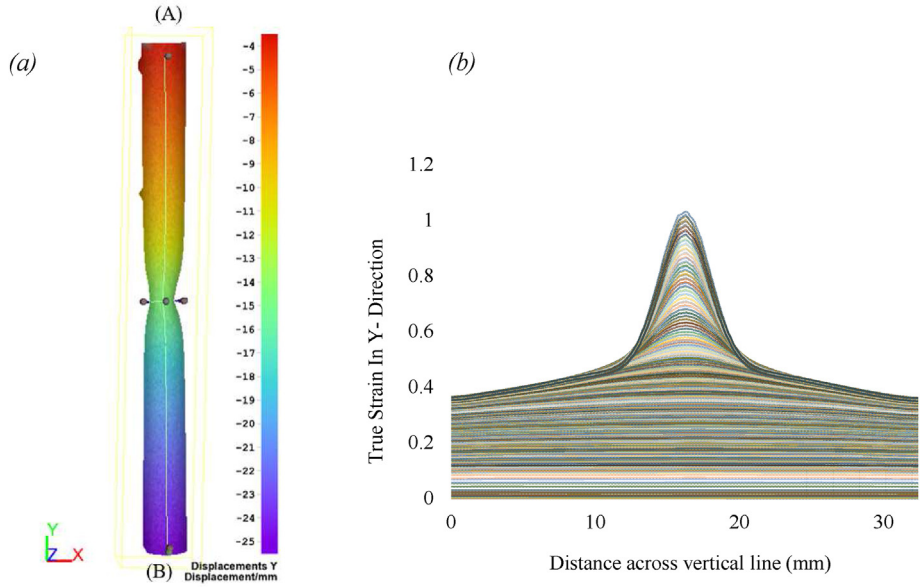

Fig. 9. a) Contour of displacement in Y-direction b)Measured true strain in Y direction against distance along the vertical line.

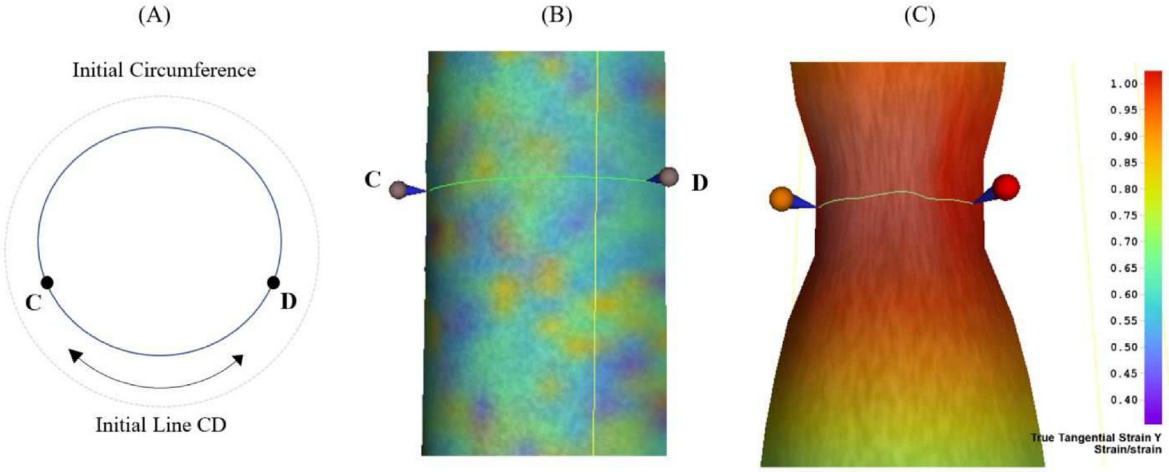

Fig. 10. Contour plot of horizontal line used to find the instantaneous cross-sectional area until failure a) line CD at step 0 b) line CD at step 269.

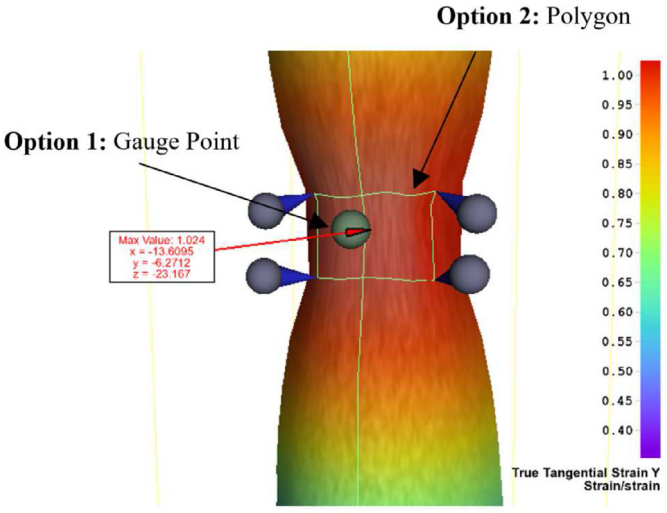

Fig. 11. Contour plot showing different gauge parameters.

load shown in the step where the onset of failure has been defined. As the DIC captures the moment before fracture, failure initiation is defined as the step before the first detectable failure crack, which aligns with the sudden drop in the load displacement curve. Thus, the accuracy of the method is dependent on the framerate, in this study a recording procedure was used which acquires frames depending on triggers set, such as time or force. The recording procedure frame rate was set at the maximum capable of the Dantec system, which was 66 frames per minute up to failure.

4.2. Anisotropy

Anisotropy is defined as the directional variation of mechanical

Table 3
Failure strains using a range gauge parameters.

Gauge Point	**Polygon -Max over surface**	Max Strain from Contour (2dp)	**Polygon -Mean over surface**	**Polygon -Min over surface**
1.0230	1.0243	1.0240	1.0236	1.0218

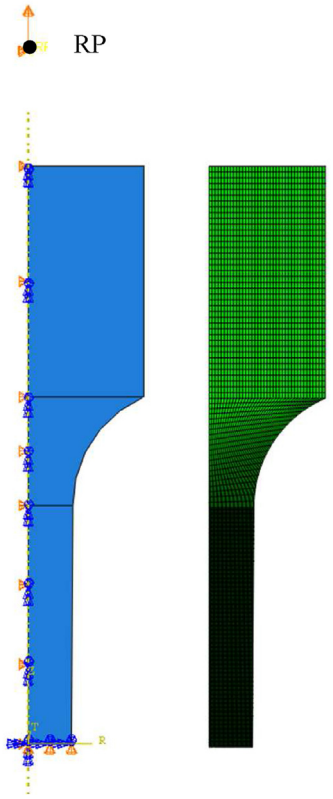

Fig. 12. Finite element model of tensile specimen.

properties. This means that the material properties may show diverse behaviours in different directions. To determine if the material being tested in this study AISI 304L is anisotropic specimens were manufactured for rolling directions; 0°, 45° and 90° (as shown in Fig. 7).

By critically evaluating the data produced, the material AISI 304L was found to be isotropic, as it did not exhibit any significant anisotropic behaviour. The graphs shown in Fig. 8 demonstrate that the results were not affected by the range of directions. The failure stresses in Fig. 8a are marginally different due to the force at which the material failed and there is no correlation between the rolling directions affecting the true stress strain curves.

4.3. Gauge parameters

When post processing DIC data it is important to use suitable gauge parameters depending on necessary requirements. There are three main data sets to be extracted from the tensile tests performed including; displacement, cross sectional area (of necking region) and true strain until the onset of failure.

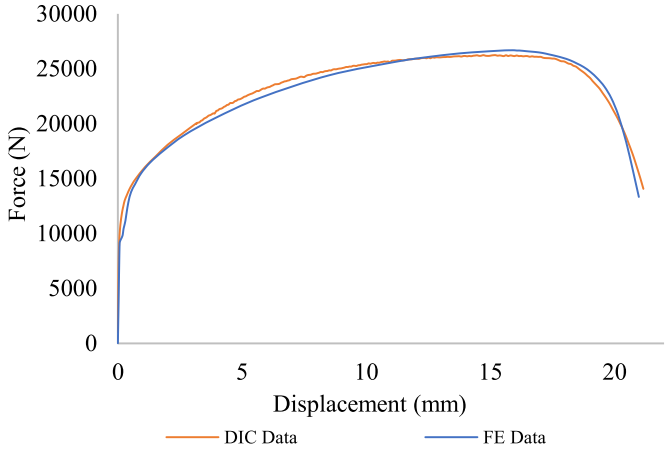

Fig. 14. Matched force displacement curves.

Displacement: Change in length of the vertical line AB as shown in Fig. 9a.

Cross Sectional Area: To calculate the true stress the actual cross-sectional area was needed. An assumption was made that the cross section of the cylindrical specimen remains as a circle during the experiment [19]. The cross sectional area of the specimen can be obtained by calculating the curvature of the surface shape with the DIC software. This has been determined by using the change in length of the horizontal line CD as shown in Fig. 10. Line CD was positioned in the region of strain localisation. Strain localisation occurs in the necked region of the specimen. The strain localisation graph in Fig. 9b was obtained using the vertical line shown in Fig. 9a and plotting the true strain in the Y direction every step until failure.

The instantaneous area was calculated by first finding the ratio between the line CD and the initial circumference, as shown in Fig. 10. The length change of line CD was extracted from the DIC data and multiplied by the ratio to determine the direct circumference. This was then used to calculate the radius. Therefore, the study was able to find the change in area throughout testing.

True Strain: Two ways of extracting true strain are shown in Fig. 11, by a gauge point and a polygon around the necking area. The maximum strain from contour is limited to 2 decimal places. The range in failure strains are shown in Table 3.

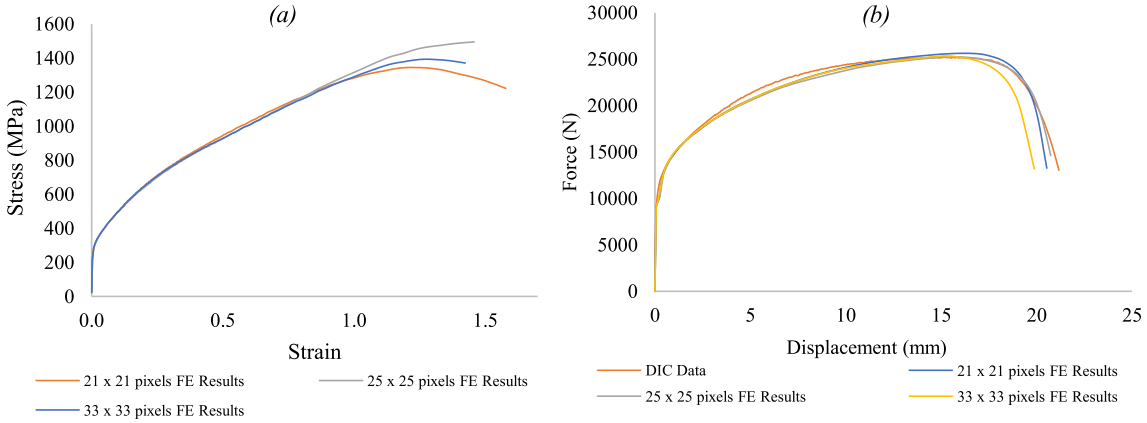

Fig. 13. a) True stress-strain curves b) force displacement curves for a range of subsets.

Table 4
Failure measurement comparisons.

	Measured Data	Original Calculated	Corrected Calculated
Failure Radius (mm)	1.70	1.73	1.68
Failure Area (mm^2)	9.03	9.41	8.90
Failure Stress (MPa)	1558	1495	1579

Using different gauge parameters has a minor effect on the strain data throughout testing. However, by using the polygon - maximum strain over surface ensures that the highest failure strain is included and this was used to extract true strain data.

4.4. Finite element model

A finite element model was built in ABAQUS/STANDARD to simulate the uniaxial tensile test using a standard von Mises plasticity model as shown in Fig. 12. An axisymmetric model was used, with symmetry boundary conditions applied along the horizontal symmetry line at the centre of the specimen, a displacement boundary condition was introduced to the remote point which was coupled to the top surface. Axisymmetric elements CAX4R were used. A mesh convergence study found the optimum number of nodes and elements were 2245 and 2096 respectively.

4.5. True stress-strain curve

Once the failure initiation and gauge parameters have been determined, true stress-strain curves can be obtained. However, as discussed previously the subset size and smoothing of data will affect the data of the parameters being extracted.

Using a range of subset sizes the true stress-strain curves have been obtained, as shown in Fig. 13a. The true stress-strain curves initially agree however, the results deviate at larger strains. The true stress-strain data for the range of subsets are used in FE analysis. The force displacement responses from the FE analysis are shown in Fig. 13b, this was compared to the experimental force displacement data (DIC Data). All of the FE analysis for various subsets underestimates the force. However, the true stress-strain data provided when using a 25 × 25 pixels subset size gives the best match and follows the experimental curve.

The ratio calculated from the original circumference and the line CD has a significant influence on the calculated area when using the direct method. The force displacement responses show that the stress should be higher than calculated.

From measuring the diameter from the failed specimen, the failure area and stress can be determined. The calculated radius at failure initiation was then compared to the actual measured value of the specimen. The original calculated area was found to be 4.2% larger than the measured area. Line CD as shown in Fig. 10c started as a circumferential line, however it does not end up as the shortest circumferential distance between points C and D, due to deformation in the necking area. In order to correct the data, the calculated ratio of the circumference was altered. Decreasing the calculated ratio increases the stress. Thus, the ratio of the circumference was iteratively reduced by 0.1%, until reaching 2.7% as the calculated force displacement curve matched the experimental force displacement curve when using a subset size of 25 × 25 pixels, as shown in Fig. 14.

Table 4 compares the original and corrected calculated failure parameters. Demonstrating the accuracy of the corrected calculated true stress-strain data.

Deformation of the FE analysis shows good agreement with the DIC image at the onset of failure. This is shown in Fig. 15 by the contours displaying true Y failure strain.

In order to demonstrate the affect for a range of local regression and smoothing spline filter, true stress-strain curve was plotted

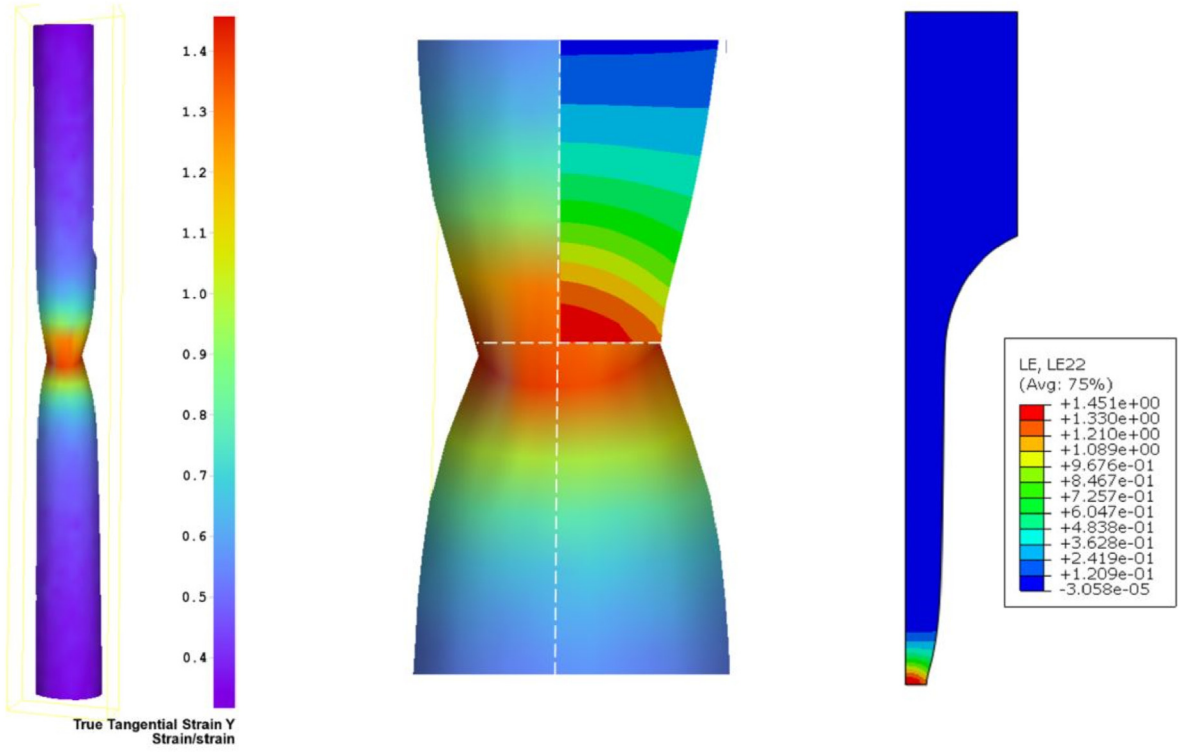

Fig. 15. Contours of True Y strain for DIC image and FE model at the onset of failure.

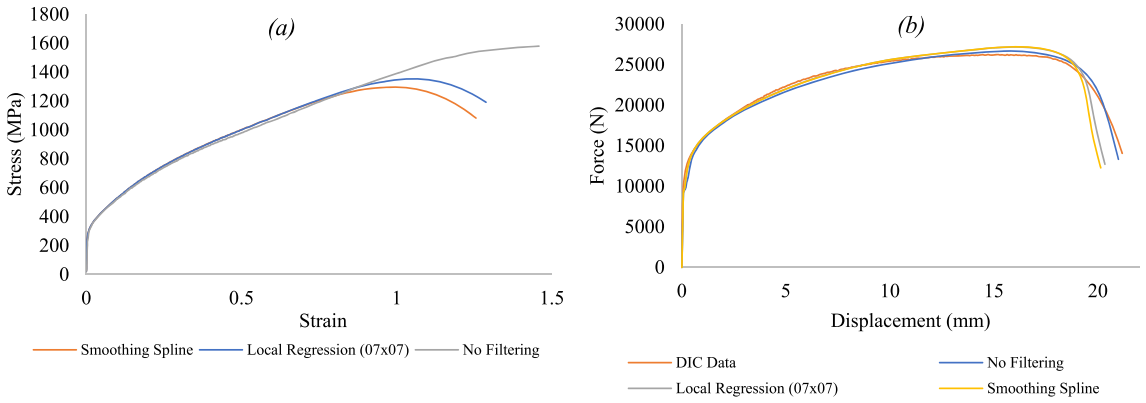

Fig. 16. a) True stress-strain curves b) force displacement curves for a range of filtering.

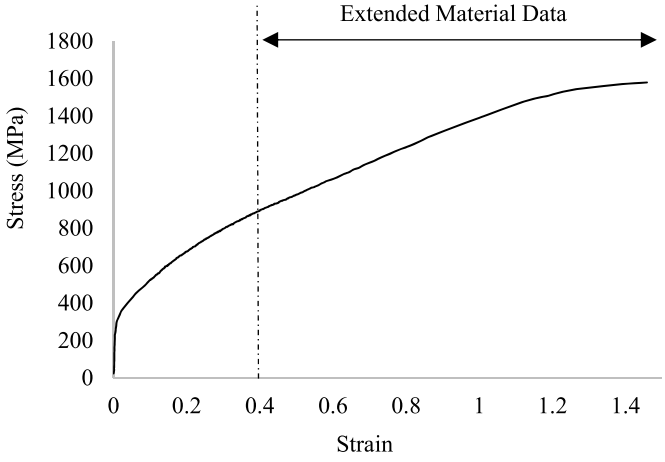

Fig. 17. Final true stress-strain data for AISI 304L.

against data when no filtering is applied, as shown in Fig. 16a. By using these sets of data in FE analysis the force displacement responses from the FE analysis are shown in Fig. 16b. This shows that as the smoothing of the data reduces the failure stress and strain the data does not predict the correct true stress-strain data. Applying any filters reduces the standard deviation of the data and decreases the spatial resolution. When the data has no filtering applied this was found to be the best match for the experimental force displacement curve.

5. Conclusion

To further understand if AISI 304L is able to withstand stringent package testing requirements, such as, impact testing, true stress strain data beyond the UTS is necessary to capture accurate data at high strains. A comprehensive literature review found precise material data for AISI 304L past UTS is deficient.

A series of uniaxial tensile tests on AISI 304L were performed. DIC was used during the experiments in order to extract data such as true strain and instantaneous cross-sectional area up to failure. The direct measurement method was used to provide true stress-strain data throughout the whole test, including beyond UTS. DIC post process study, investigated the effect of using different filtering and subset size results when producing true stress-strain data. FE analysis was executed using the different true stress-strain data sets to compare the force displacement responses. In this study, it was found that the post processing of the DIC software significantly influenced the extracted data. A subset size of 25 × 25 pixels and no filtering, produced true stress-strain data that was in agreement with the experimental results, as shown in Fig. 17. The tabulated data points for yield stress and plastic strain are shown in Appendix A. The vertical line shown on Fig. 17 shows the upper strain limit which can be obtained before non-uniform deformation takes place. The work presented in this paper has indicated a general methodology to be adopted, but has also provided accurate extended material data beyond UTS for AISI 304L.

Declaration of competing interest

The authors declare that they have no known competing financial interests or personal relationships that could have appeared to influence the work reported in this paper.

Acknowledgements

The support from the European Union's Horizon 2020 research and innovation program under the Marie Skłodowska-Curie grant agreement (No 823786) is acknowledged.

Appendix A

Yield Stress (MPa)	Plastic Strain
215.59	0.000
290.07	0.010
483.06	0.080
556.50	0.120
590.89	0.140
622.92	0.162
653.53	0.183
682.15	0.205
708.99	0.225
734.56	0.245
759.18	0.266
783.12	0.288
806.37	0.309
828.84	0.331
851.52	0.354
874.43	0.377
897.88	0.403
922.68	0.432
950.04	0.465
983.21	0.505
1032.92	0.562
1126.23	0.672
1286.69	0.865
1501.56	1.205
1579.15	1.458

References

[1] Pacific Nuclear Transport Limited, Packages, 2021 accessed Mar. 15, 2021, https://www.pntl.co.uk/safety/packages/.

[2] International Atomic Energy Agency, Regulations for the Safe Transport of Radioactive Material, 2018 Edition, 2018 [Online]. Available: http://www-ns.iaea.org/standards/.

[3] K. Zhao, L. Wang, Y. Chang, J. Yan, Identification of post-necking stress-strain curve for sheet metals by inverse method, Mech. Mater. 92 (Jan. 2016) 107–118, https://doi.org/10.1016/j.mechmat.2015.09.004.

[4] M.S. Joun, J.G. Eom, M.C. Lee, A new method for acquiring true stress-strain curves over a large range of strains using a tensile test and finite element method, Mech. Mater. 40 (7) (Jul. 2008) 586–593, https://doi.org/10.1016/j.mechmat.2007.11.006.

[5] M. Dunand, D. Mohr, Hybrid experimental-numerical analysis of basic ductile fracture experiments for sheet metals, Int. J. Solid Struct. 47 (9) (May 2010) 1130–1143, https://doi.org/10.1016/j.ijsolstr.2009.12.011.

[6] L. Wang, W. Tong, Identification of post-necking strain hardening behavior of thin sheet metals from image-based surface strain data in uniaxial tension tests, Int. J. Solid Struct. 75 (76) (Dec. 2015) 12–31, https://doi.org/10.1016/j.ijsolstr.2015.04.038.

[7] M. Kamaya and M. Kawakubo, "A Procedure for Determining the True Stress-Strain Curve over a Large Range of Strains Using Digital Image Correlation and Finite Element Analysis," doi: 10.1016/j.mechmat.2011.02.007.

[8] H.W.S. Sutton, A. Michael, Orteu Jean-José, Image Correlation for Shape, Motion and Deformation Measurements, No. 2009, Boston, MA: Springer US, 2009.

[9] P. Hariharan, Interferometry, in: Optical Interferometry, Elsevier, 2003, pp. 1–8.

[10] W.H. Peters, W.F. Ranson, Digital imaging techniques in experimental stress analysis, Opt. Eng. 21 (3) (Jun. 1982), https://doi.org/10.1117/12.7972925.

[11] M. Sutton, C. Mingqi, W. Peters, Y. Chao, S. McNeill, Application of an optimized digital correlation method to planar deformation analysis, Image Vis Comput. 4 (3) (1986) 143–150, https://doi.org/10.1016/0262-8856(86)90057-0.

[12] M.A. Sutton, J. Yan, Computer vision for shape and deformation measurements: recent developments and applications, SAE Tech. Pap. 115 (2006) 495–500, https://doi.org/10.4271/2006-01-0526.

[13] Y. Bai, Effect of Loading History in Necking and Fracture Architected Materials Design and Fabrication Using Additive Manufacturing View Project [Online]. Available: https://www.researchgate.net/publication/38003378.

[14] D. Mohr, M. Oswald, A new experimental technique for the multi-axial testing of advanced high strength steel sheets, Exp. Mech. 48 (1) (2008) 65–77, https://doi.org/10.1007/s11340-007-9053-9.

[15] M. Dunand, D. Mohr, Optimized butterfly specimen for the fracture testing of sheet materials under combined normal and shear loading, Eng. Fract. Mech. 78 (17) (2011) 2919–2934, https://doi.org/10.1016/j.engfracmech.2011.08.008.

[16] H. Ghadbeigi, C. Pinna, S. Celotto, Failure mechanisms in DP600 steel: initiation, evolution and fracture, Mater. Sci. Eng. A 588 (Dec. 2013) 420–431, https://doi.org/10.1016/j.msea.2013.09.048.

[17] J. Li, G. Yang, T. Siebert, M.F. Shi, L. Yang, A method of the direct measurement of the true stress–strain curve over a large strain range using multi-camera digital image correlation, Opt Laser. Eng. 107 (Aug. 2018) 194–201, https://doi.org/10.1016/j.optlaseng.2018.03.029.

[18] P.D. Versaillot, Y.F. Wu, Z.L. Zhao, Experimental study on the evolution of necking zones of metallic materials, Int. J. Mech. Sci. 189 (Jan. 2021) 106002, https://doi.org/10.1016/j.ijmecsci.2020.106002.

[19] F. Zhu, P. Bai, J. Zhang, D. Lei, X. He, Measurement of true stress-strain curves and evolution of plastic zone of low carbon steel under uniaxial tension using digital image correlation, Opt Laser. Eng. 65 (Feb. 2015) 81–88, https://doi.org/10.1016/j.optlaseng.2014.06.013.

[20] H.C. Ho, K.F. Chung, X. Liu, M. Xiao, D.A. Nethercot, Modelling tensile tests on high strength S690 steel materials undergoing large deformations, Eng. Struct. 192 (November 2018) 305–322, https://doi.org/10.1016/j.engstruct.2019.04.057, 2019.

[21] S. Yaofeng, J.H.L. Pang, Study of optimal subset size in digital image correlation of speckle pattern images, Opt Laser. Eng. 45 (9) (2007) 967–974, https://doi.org/10.1016/j.optlaseng.2007.01.012.

[22] J. Baldoni, G. Lionello, F. Zama, L. Cristofolini, Comparison of different filtering strategies to reduce noise in strain measurement with digital image correlation, J. Strain Anal. Eng. Des. 51 (6) (2016) 416–430, https://doi.org/10.1177/0309324716646690.

[23] S. Yoneyama, Basic principle of digital image correlation for in-plane displacement and strain measurement, Adv. Compos. Mater. 25 (2) (Mar. 2016) 105–123, https://doi.org/10.1080/09243046.2015.1129681.

[24] W. Tong, An evaluation of digital image correlation criteria for strain mapping applications, Strain 41 (4) (2005) 167–175, https://doi.org/10.1111/j.1475-1305.2005.00227.x.

[25] B. Pan, H. Xie, Z. Wang, Equivalence of digital image correlation criteria for pattern matching, Appl. Opt. 49 (28) (2010) 5501–5509, https://doi.org/10.1364/AO.49.005501.

[26] B. Pan, Digital image correlation for surface deformation measurement: historical developments, recent advances and future goals, Meas. Sci. Technol. 29 (8) (2018), https://doi.org/10.1088/1361-6501/aac55b.

[27] P. Reu, Stereo-rig design: creating the STEREO-RIG LAYOUT - PART 1, Exp. Tech. 36 (5) (2012) 3–4, https://doi.org/10.1111/j.1747-1567.2012.00871.x.

[28] P. Reu, All about speckles: speckle density, Exp. Tech. 39 (3) (2015) 1–2, https://doi.org/10.1111/ext.12161.

[29] P. Reu, Speckles and their relationship to the digital camera, Exp. Tech. 38 (4) (2014) 1–2, https://doi.org/10.1111/ext.12105.

[30] R. Huňady, M. Hagara, M. Kalina, The aspects of strain fields' measurement performed on small surfaces using digital image correlation method, EAN 2014 - 52nd Int. Conf. Exp. Stress Anal. 1 (June, 2014) 334–342.

[31] Y. Wang, S. C. Garcea, and P. J. Withers, "7.6 Computed Tomography of Composites," doi: 10.1016/B978-0-12-803581-8.10250-4.

[32] L.S. Athanasiou, D.I. Fotiadis, L.K. Michalis, Propagation of segmentation and imaging system errors, in: Atherosclerotic Plaque Characterization Methods Based on Coronary Imaging, Elsevier, 2017, pp. 151–166.

[33] R.K. Blandford, D.K. Morton, S.D. Snow, T.E. Rahl, Tensile Stress-Strain Results for 304L and 316L Stainless Steel Plate at Temperature 2007 ASME Pressure Vessels and Piping Division Conference TENSILE STRESS-STRAIN RESULTS for 304L and 316L STAINLESS STEEL 1 PLATE at TEMPERATURE, 2007.

[34] R. Bigger, et al., A Good Practices Guide for Digital Image Correlation, Oct. 2018, https://doi.org/10.32720/idics/gpg.ed1.

[35] P. Reu, Hidden components of DIC: calibration and shape, Function-Part 1 (2012).

[36] British Standards Institution, BSI Standards Publication Testing Hardened Concrete, vol. 18, 2019.

[37] L. Xue, Damage accumulation and fracture initiation in uncracked ductile solids subject to triaxial loading, Int. J. Solid Struct. 44 (16) (Aug. 2007) 5163–5181, https://doi.org/10.1016/j.ijsolstr.2006.12.026.

[38] Y. Bao, T. Wierzbicki, On fracture locus in the equivalent strain and stress triaxiality space, Int. J. Mech. Sci. 46 (1) (Jan. 2004) 81–98, https://doi.org/10.1016/j.ijmecsci.2004.02.006.

[39] S. Baltic, J. Magnien, H.P. Gänser, T. Antretter, R. Hammer, Coupled damage variable based on fracture locus: modelling and calibration, Int. J. Plast. 126 (Mar. 2020) 102623, https://doi.org/10.1016/j.ijplas.2019.11.002.